RESEARCH ARTICLE

Seismic control performance of a three-story frame prototype equipped with semi-active variable stiffness and damping structural joints

Qinyu Wang[1] | Gennaro Senatore[2] | Kaspar Jansen[3] | Arjan Habraken[1] |
Patrick Teuffel[1]

[1] Chair of Innovative Structural Design, TU Eindhoven, Eindhoven, The Netherlands

[2] Applied Computing and Mechanics Laboratory, Swiss Federal Institute of Technology, Lausanne, Switzerland

[3] Department of Design Engineering, TU Delft, Delft, The Netherlands

Correspondence
Qinyu Wang, Chair of Innovative Structural Design, TU Eindhoven, Eindhoven, The Netherlands.
Email: q.wang2@tue.nl

Qinyu Wang and Gennaro Senatore contributed equally to this work.

Abstract

This paper presents numerical and experimental studies on semi-active seismic response control of structures equipped with variable stiffness and damping structural joints. Such adaptive joints, which are comprised of a shape memory polymer (SMP) core reinforced by an SMP-aramid composite skin, function as load-transfer components as well as semi-active control devices. The SMP core material can transition from a glassy to a rubbery state through thermal actuation resulting in a shift of the structural natural frequencies and a parallel increase of damping ratio, which enables a new semi-active control strategy. Control performance has been evaluated on a three-story frame equipped with 12 adaptive joints and subjected to seismic excitations. Full-transient analysis has shown that when the joints are thermally actuated to the transition temperature (65°C), acceleration and base shear are reduced by up to 62% and 65%, respectively. Shake-table tests have been carried out on a 1/10-scale prototype, confirming that through thermal actuation of the adaptive joints the structural damping ratio increases from 2.6% to 11.3% and the first natural frequency shifts by up to 37%. As the structure becomes more flexible, an increase of displacements and interstory drift might occur. However, depending on the seismic excitation, top-story acceleration and base shear are significantly reduced in the range 43%–50% and 35%–51%, respectively. These results confirm that semi-active control through thermal actuation of variable stiffness and damping structural joints is effective to mitigate the structure response under seismic excitation.

KEYWORDS
adaptive structures, seismic response control, semi-active control, shake-table test, variable stiffness and damping, viscoelastic material

1 | INTRODUCTION

1.1 | Previous work

Adaptive structures are equipped with sensing, actuation, and control systems to operate optimally under changing load conditions and other environmental actions. Structural control strategies have been categorized into four main types: passive, active, semi-active, and hybrid.[1–3] Passive control systems typically reduce the structure response through either base isolation devices[4] or energy dissipation devices such as viscoelastic and elastoplastic dampers.[5] Passive control systems require no input energy because control forces are developed through the motion of the structure. Active control systems, for example, active mass dampers and active bracing systems, provide control forces through actuation based on feedback from sensors that measure the structure response. Numerical and experimental studies have shown that active control systems are more effective than passive systems to mitigate the response of seismic- and wind-excited buildings.[6–9] However, active control systems typically require a high power density supply and need scheduled maintenance. In addition, measurement and modeling inaccuracy might, in some cases, cause instability of the structure-control system.[10] Semi-active control systems are generally reliable and retain some of the capabilities of active systems while requiring a small external power source for operation.[2,11,12] Control forces are developed as a result of the structure motion through controlled changes of the mechanical properties of semi-active control devices such as magnetorheological and electrorheological dampers,[13,14] as well as variable stiffness and damping devices.[15,16] Hybrid control systems typically combine passive and active or semi-active control strategies and devices (e.g., hybrid mass dampers). While hybrid control systems are effective to control the dynamic response under a wide range of loading scenarios, such systems are generally complex and may require significant maintenance costs.[17]

Optimal integration of sensing and actuation capabilities enable structures to counteract the effect of loading actively through control of internal forces and structural shape. Well-designed adaptive structures are able to operate closer to design limits with a better material utilization[18–20] as well as significantly lower whole-life energy[21,22] compared to conventional passive structures. Whole-life energy minimization is a design criterion that accounts for the energy embodied (or embodied carbon equivalent) in the material and the operational share for active control. Numerical and experimental studies have shown that well-designed adaptive structures achieve significant whole-life energy savings (up to 70%) compared to weight-optimized passive structures thus minimizing adverse environmental impacts.[23–26]

Structural adaptation requires flexibility of the joints to prevent stress build-up, which could cause damage, reduce control accuracy, and increase control effort. However, as joints are load-transfer components, strength and serviceability requirements must be met. To address these conflicting requirements, adaptive joints that have variable stiffness properties have been investigated.[27] Such adaptive joint can transition from a "locked" to a "released" state (moment to pin connection) through a change of stiffness controlled through thermal actuation. Design and characterization of a variable stiffness and damping structural joint made of a polyurethane-based shape memory polymer (SMP) has been carried out in (Wang et al 2020a).[28] Dynamic mechanical analysis (DMA) tests have shown that the joint core material features a significant stiffness reduction through thermal actuation and a parallel increase of damping caused by viscoelastic effects. This property change has been employed in (Wang et al. 2020b)[29] to investigate a new semi-active control strategy for truss and frame structures equipped with variable stiffness and damping joints. Vibration control simulations of a truss bridge and a four-story frame subjected to resonance, moving, and earthquake loading have shown that through thermal actuation of the adaptive joints, it is possible to cause a shift of the structure natural frequencies and to increase the damping ratio, which results in a significant reduction by up to 95% of the acceleration peak amplitude.

Semi-active strategies based on stiffness and damping control mitigate the structure response through appropriate adjustment of the structural dynamic properties.[30–32] Existing stiffness and damping control systems comprise several parts and generally require complex detailing for installation. In addition, existing devices are effective within specific conditions such as limited yield displacements and they require damping provided by external means.[31,32] Compared to existing solutions, the adaptive joints investigated in this work are simpler semi-active control devices that do not involve complex mechanisms based on moving parts because they are controlled through thermal actuation (solid state). The actuation mechanism is inherent within the properties of the material enabling a reliable control system that is able to perform adequately under a wide range of conditions. In addition, as adaptive joints can be fabricated through 3D printing and are load-transfer components, they can be well integrated into most structural systems.

1.2 | New contribution

This paper builds on and expands the work carried out in (Wang et al. 2020a; Wang et al. 2020b)[28,29], which focused on material characterization and numerical simulations, by providing an experimental assessment of semi-active seismic response control through thermal actuation of variable stiffness and damping structural joints. More specifically, this work offers the following new contributions:

- Detailed design of a 1/10-scale prototype equipped with 12 adaptive joints, which includes element sizing, joint detailing, thermal actuation system, motion control system (shake table), and data acquisition system.
- Frequency shift and damping increase caused by thermal actuation of the adaptive joints are measured through free vibration tests.
- Semi-active response control through shake-table tests under four different seismic excitations. Control performance is quantified through 10 evaluation criteria including maximum and normed story acceleration, story displacement, interstory drift and base shear.
- Experimental results are benchmarked against numerical predictions. A response spectrum analysis is carried out to uncouple the effect of frequency and damping variation on the structure response.
- The effects of scaling and actuation time delay on control performance are investigated through numerical studies by comparing the response of the 1/10-scale model with that of its corresponding full-scale model.

1.3 | Outline

This paper is arranged into seven sections. Section 2 gives an outline of the proposed adaptive joint design and semi-active vibration control strategy. Sections 3 presents numerical studies on a 1/10-scale three-story frame equipped with 12 adaptive joints and subjected to four seismic loadings. Section 4 presents experimental results obtained through shake-table tests. In Section 5, a numerical study is carried out on the full-scale three-story frame structure to evaluate the effects of scaling and control time delays. Section 6 and Section 7 conclude this paper.

2 | VIBRATION CONTROL THROUGH ADAPTIVE STRUCTURAL JOINTS

2.1 | Joint design

The variable stiffness and damping structural joint proposed in this work, which is referred to as "adaptive joint" hereafter, consists of a SMP core that is reinforced by an SMP-aramid composite skin. Figure 1 shows one of the adaptive joints that has been fabricated for the 1/10-scale three-story frame prototype described in Section 4.1. The joint core shown in Figure 1A has been made through 3D printing. A continuous resistive heating wire is passed through a series of holes that have been made through selective deposition. The joint core is connected to four aluminum tubes (Figure 1B) through structural glue (Pattex 100%). A reinforcement skin is then applied to the joint-tube assembly Figure 1C. The reinforcement skin has two functions: (a) to limit deformations under loading when the joint core stiffness is reduced through thermal
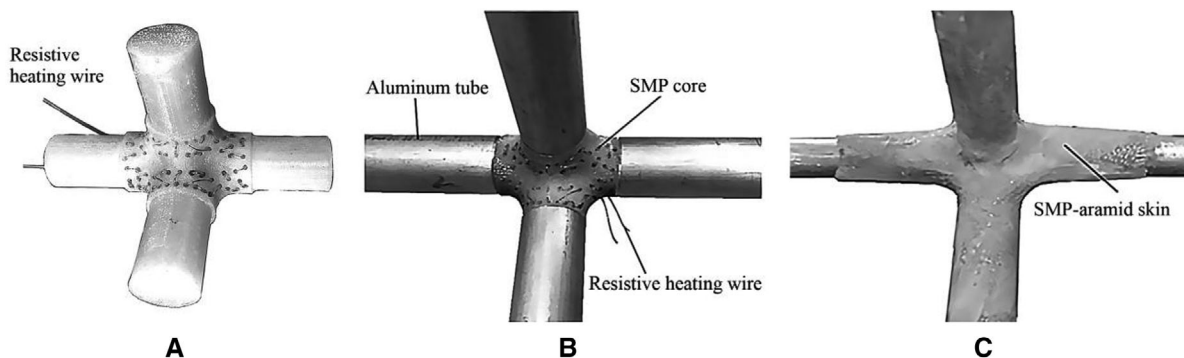

FIGURE 1 (A) SMP joint core; (B) joint connected to four aluminum tubes; (C) SMP-aramid skin[29]

actuation, and (b) to strengthen the connection of the joint with structural elements. The reinforcement skin is the part of the joint that takes most of the stress, which is the highest when the joint is thermally actuated owing to the core stiffness reduction. The reinforcement skin consists of a stack of woven aramid fabric layers, which are impregnated within an SMP resin to form a stiff and thin composite. Because structural joints generally have a complex geometry and are typically subjected to forces from multiple directions including bending and torsion, the skin composite has been designed to have isotropic behavior. Two layers having ±45° fiber orientation are sandwiched between two layers with 0°/90° fiber orientation to form a four-layer stack with a thickness of 1.72 mm. An average modulus and ultimate stress of 8320 MPa and 107 MPa, respectively, have been measured through tensile testing.[28] Depending on the worst-case loading condition, a stronger reinforcement skin can be obtained by stacking more layers.

2.2 | Material characterization and modeling

SMPs are able to transition from a glassy to a rubbery state through actuation (e.g., thermal, magnetic). Below the transition temperature T_g, the polymer is relatively stiff having a modulus of approximately 1 GPa whereas above T_g, the polymer has a rubbery elastic behavior with a modulus reduced by approximately 1000 times.[33] The thermomechanical properties of the SMP joint core material (MM5520, *SMP Technologies Inc.*) have been characterized through DMA in (Wang et al. 2020a).[28] Figure 2A shows the plot of storage modulus E', loss modulus E'' and tan δ as functions of the temperature at a strain rate of 1 Hz. The storage modulus characterizes the elastic behavior in which strain and stress are in phase. When either in the glassy or rubbery state, SMP behaves elastically. When the material enters the viscoelastic region, strain and stress go out of phase. Energy dissipation through heating due to friction is characterized by the loss modulus E''. The ratio tan $\delta = E''/E'$ is a measure of damping.[34,35] Note that during state transition (from 50°C to 65°C), the modulus drops from 1340 to 37 MPa. The elastic stiffness reduces by 96% while damping increases 11-fold.

Two material models have been developed in (Wang et al. 2020a)[28]: thermo-elastic and viscoelastic. The thermo-elastic model is a simplified material model, which takes the storage modulus curve at 1 Hz (Figure 2) while ignoring damping variation due to viscoelastic effects. The viscoelastic material model instead characterizes stiffness and damping variation with temperature and strain rate (i.e., frequency). Time-temperature superposition principle has been applied to map experimental data obtained at different temperatures and frequencies onto a single master curve[28] that is shown in Figure 2B.

The structure natural frequency shift that occurs when the joints are thermally actuated is caused primarily by the joint stiffness reduction, and thus viscoelastic effects can be neglected. For this reason, the thermo-elastic model is employed in modal analysis to evaluate the structure natural frequency shift with temperature as well as to analyze the uncontrolled response, that is, the joints are not thermally actuated and are assumed to have a temperature of 25°C (the core material is elastic). The viscoelastic material model is employed to analyze the controlled response in the temperature range 40°C to 65°C to appreciate the simultaneous effect of frequency and damping variation caused by stiffness reduction and viscoelasticity, respectively.
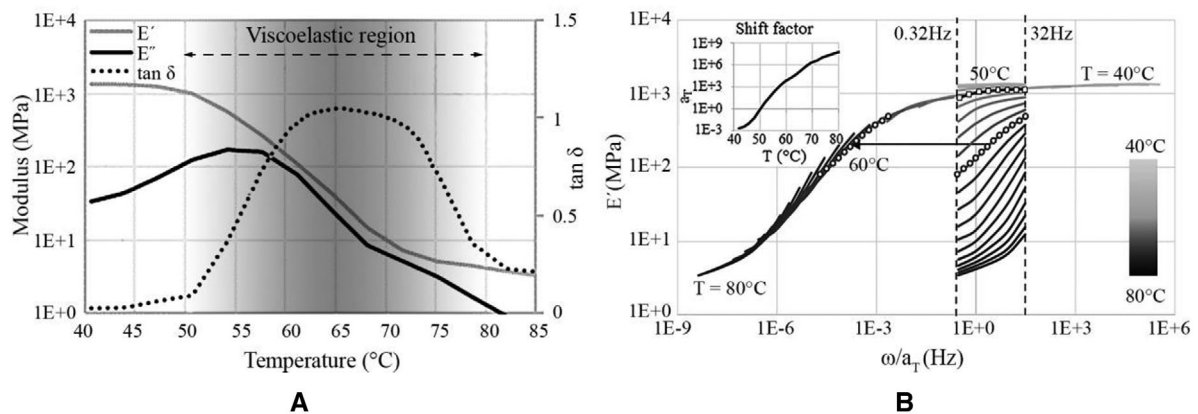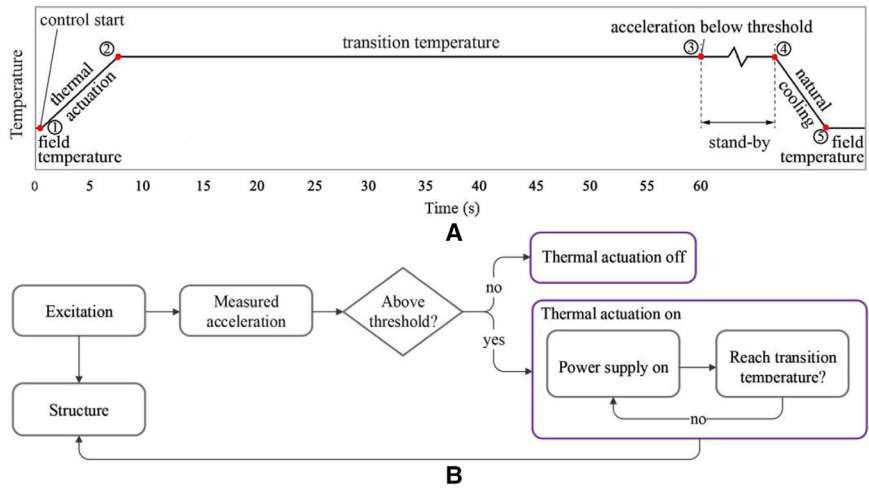

FIGURE 2 SMP material characterization through DMA: (A) storage modulus (E'), loss modulus (E''), and material damping (tan δ) versus temperature at 1 Hz; (B) master curve[28]

FIGURE 3 (A) Temperature control law;
(B) control strategy flowchart[29]

2.3 | Semi-active feedforward control

For structures that are equipped with adaptive joints, the change of material properties that occur in the transition phase triggered by thermal actuation induces a shift of natural frequencies and an increase of damping ratio. Numerical simulations have shown that such frequency shift and damping increment can be effectively employed to mitigate the structure response under dynamic excitations.[29] Under excitations that have several high-energy frequency components (e.g., earthquakes), although a temporary resonance condition may occur in some cases due to the structure frequency shift, the effect of damping increment is dominant when the joints are actuated to the transition temperature.

From material characterization (tan δ curve in Figure 2A), it is clear that the increase of damping ratio is the highest when the joint core material is thermally actuated to the transition temperature. For this reason, a simple feedforward control scheme is proposed. Assume a multistory building equipped with adaptive joints and subjected to a generic ground motion. Accelerometers are installed at the ground level and on each floor. Figure 3A shows the temperature control law for the joints. Thermal actuation of the joints is switched on when the ground acceleration becomes higher than a set threshold (point 1). The transition temperature of the joint core is set as the target control temperature. Once the joint temperature reaches the transition value (point 2), the temperature is kept constant. The temperature control process of the joint is regulated independently through a feedback control system (Section 4.2). The response of the structure is reduced through the combined effect of frequency shift and damping ratio increment. Once the ground acceleration reduces below the set threshold (point 3), the joint temperature is kept at the transition value for a certain period (standby) after which, if no further increase of acceleration is measured, thermal actuation is switched off (point 4). Then, the joint temperature reduces to the field temperature through natural cooling (point 5). Figure 3B shows a schematic flowchart of the feedforward control scheme including the closed feedback loop for joint temperature modulation.

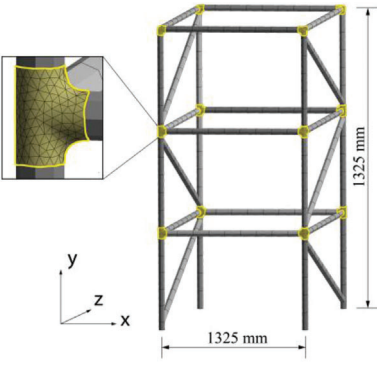## 3 | NUMERICAL STUDY ON A 1/10-SCALE THREE-STORY FRAME

3.1 | Structural design

The experimental prototype developed in this work is a 1/10-scale three-story building with dimensions 1325 × 650 × 650 mm as indicated in Table 1. The frame is made of aluminum tube elements connected through 12 adaptive joints (all nodes except the supports). As the structure is subjected to one-dimensional ground motion along the x direction (Section 4.1), diagonal bracings are installed in the zy plane to limit torsional effects. The outer diameter and wall thickness of all aluminum tubes are 25 and 2.5 mm, respectively. All adaptive joint cores have been 3D printed while the reinforcement skin has been applied manually. Each floor supports five steel weights (51 kg) housed on a wooden plate (4 kg), which is equivalent to a dead load of 150 kg/m^2.

The frame structure is modeled through finite elements in Ansys Workbench. Table 1 shows the FEM model including a close-up of the joint mesh. Each aluminum tube is modeled with nine beam elements (BEAM188) and each joint with approximately 2690 solid elements (SOLID186). The beam elements connect to the joint through a section perpendicular to their axis as indicated by the yellow contouring in Table 1. The beam sections connect to the joint elements through a

TABLE 1 1/10-Scale model (simulation): Frequency and damping variation for first and second modes

	25°C	40°C	45°C	50°C	55°C	60°C	65°C
ω_1^s (Hz)	3.20	3.16	3.15	3.09	2.88	2.59	2.31
ω_2^s (Hz)	10.5	10.4	10.4	10.2	9.57	8.77	8.05
$S_{\omega 1}^s$ (%)	–	1.1	1.5	3.4	10.0	19.1	27.7
$S_{\omega 2}^s$ (%)	–	1.1	1.4	3.1	8.8	16.5	23.3
ζ^s (%)	2.6	2.6	2.6	3.0	4.6	7.6	9.5

FEM model

fixed contact. The isotropic SMP-aramid skin is modeled with shell elements (SHELL281) with a thickness of 3 mm that is obtained by stacking eight aramid fabric layers of the SMP-aramid composite described in Section 2.1. For simplicity, as the reinforcement skin is applied on the outer surface of the joint, it is assumed that the skin will behave as an elastic material.

3.2 | Frequency shift and damping ratio variation through joint thermal actuation

Thermal actuation of the adaptive joints causes an overall stiffness reduction, which results in a shift of the structure natural frequencies. In parallel, the joint core material transitions into the viscoelastic region, which causes an increase of the structure damping ratio. As discussed in Section 2.2, because the frequency shift is caused primarily by the joint stiffness reduction (i.e., viscoelastic effects can be neglected), it is evaluated through modal analysis using the thermo-elastic material model. Instead, the damping ratio variation is evaluated through free vibration tests that are simulated through full transient analysis using the viscoelastic material model.

First and second modes are observed. The joints are actuated from ambient (25°C) to transition temperature (65°C) in discrete steps through a time-constant thermal load. Natural frequency and frequency shift for first and second modes are given in Table 1. The structure frequency reduces as the joint temperature increases owing to the stiffness reduction of the joints. The first and second mode frequency shifts are $S_{\omega 1}^s$ = 27.7% and $S_{\omega 2}^s$ = 23.3%, respectively, as the joint temperature reaches the transition value. The superscript s stands for "scaled model."

A free vibration test is simulated by applying a 1 N impulse load in the x-direction (see axis in Table 1) to the middle of the top-story left side beam. The joints are actuated from ambient (25°C) to transition temperature (65°C) in discrete steps. Each vibration test is carried out for a period of 20 s. At ambient temperature, the structure damping ratio is set to 2.6% as measured through experimental testing (Section 4.3). Note that for $T \leq 40°C$, the joint core material behaves elastically because it is in the glassy state and thus the contribution to the structure damping ratio due to viscoelastic effects is negligible (see Figure 2A, tan δ is approximately 0 at $T = 40°C$). When performing a full transient analysis, the structure damping ratio is also affected by frequency shift. However, the objective of this analysis is to evaluate the change of structure damping due to viscoelastic effects caused by thermal actuation of the joints. For this reason, an extended Rayleigh damping model given by Equation (1)[36] is employed to minimize the damping ratio variation due to frequency shift between the range defined by the first mode frequency at ambient temperature (25°C) and that at the transition temperature (65°C). The mass coefficient α and stiffness coefficient β are computed through Equation (2), where h_{aim} = 2.6% is the target damping ratio as in Table 1. The coefficients α and β are 0.41 and 1.53e^{-3}, respectively. For clarity, Figure 4 shows the Rayleigh damping ratio as a function of structure frequency. The maximum Rayleigh damping variation caused by frequency shift is minimized to 0.09% (from 2.6% to 2.51%), which is a 3% error compared with the target damping ratio (2.6%).

$$\zeta_r = \frac{\alpha}{2\omega} + \frac{\beta\omega}{2}, \tag{1}$$

$$\alpha = \frac{2h_{aim}\omega_1 \omega_2}{\omega_1 + \omega_2}, \quad \beta = \frac{2h_{aim}}{\omega_1 + \omega_2}. \tag{2}$$
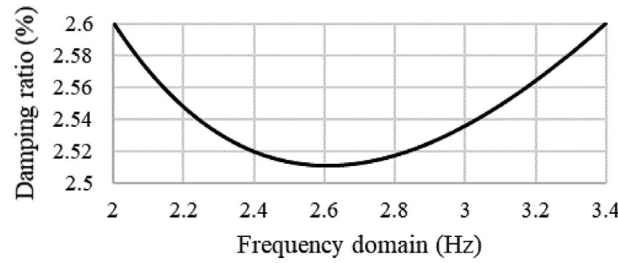
FIGURE 4 Extended Rayleigh damping

Table 1 gives the structure damping ratio for each temperature. The damping ratio ζ has been computed from the displacement logarithmic decrement $\Delta = \ln(x_3(t)/x_3(t+1))$ as

$$\zeta = \frac{\Delta/2\pi}{\sqrt{1 + (\Delta/2\pi)^2}}, \tag{3}$$

where $x_3(t)$ is the top-story (third story) average displacement. The increase of material damping due to viscoelastic effects caused by thermal actuation of the joints results in a significant 3.6-fold increase of the structure damping ratio from 2.6% at ambient temperature (25°C) to 9.5% at transition temperature (65°C).

3.3 | Seismic loading

Four seismic loadings have been selected for numerical simulation and experimental testing: (a) 1940 El Centro (USA); (b) 1995 Kobe (Japan), (c) 1999 Chichi (Taiwan), and (d) 1999 Kocaeli (Turkey). As the structure considered in this study is scaled by a factor of $\lambda = 1/10$, the external loading must be scaled appropriately to ensure that the 1/10-scale model response is comparable with that of the full-scale model. To do so, the ratio between excitation and structure frequency components must be the same for scaled and full-scale models. From laws of similitude, the seismic loading frequency is scaled by $\lambda_\omega = \lambda^{-1/2} = 3.16$ with respect to the original record, while the acceleration is not scaled $\lambda_a = 1$.[37] This way the 1/10-scale model is subjected to the same ground acceleration compared with the full-scale model. All seismic loadings are applied along the x direction in the xy plane (Table 1).

3.4 | Semi-active seismic response control through adaptive structural joints

3.4.1 | Evaluation criteria

Control performance is assessed with five evaluation criteria that are related to maximum response (Equations 4–12) as well as normed response (Equations 5–13). The control performance criteria on story displacement (J_1–J_{1n}), interstory drift ratio (J_2–J_{2n}), story acceleration (J_3–J_{3n}), and base shear (J_4–J_{4n}) are taken from Ohtori et al.[6] An additional evaluation criterion has been formulated to evaluate the stress response of the reinforcement skin (J_5–J_{5n}), which takes most of the stress owing to the joint core stiffness reduction caused by thermal actuation. All evaluation criteria compare the controlled response (indicated by the superscript c) with the uncontrolled response under each seismic excitation. The average acceleration and displacement among all degrees of freedom for each story are considered representative of the structure dynamic response.

$$J_1 = \frac{\max_t \left| x_i^c(t) \right|}{x_i^{\max}}, \tag{4}$$

$$J_{1n} = \frac{\| x_i^c(t) \|}{\| x_i \|}, \tag{5}$$

$$J_2 = \frac{\max_t \frac{|d_i^c(t)|}{h_i}}{\rho_i^{\max}}, \tag{6}$$

$$J_{2n} = \frac{\frac{\|d_i^c(t)\|}{h_i}}{\|\rho\|}, \tag{7}$$

$$J_3 = \frac{\max_t |\ddot{x}_i^c(t)|}{\ddot{x}^{\max}}, \tag{8}$$

$$J_{3n} = \frac{\|\ddot{x}_i^c(t)\|}{\|\ddot{x}\|}, \tag{9}$$

$$J_4 = \frac{\max_t \left|\sum_i m_i \ddot{x}_i^c(t)\right|}{F_b^{\max}}, \tag{10}$$

$$J_{4n} = \frac{\left\|\sum_i m_i \ddot{x}_i^c(t)\right\|}{\|F_b\|}, \tag{11}$$

$$J_5 = \frac{\max_{t,j} |\sigma_j^c(t)|}{\sigma^{\max}}, \tag{12}$$

$$J_{5n} = \frac{\|\sigma_j^c(t)\|}{\|\sigma\|}, \tag{13}$$

where

- $i = [1,2,3]$ indicates the story number;
- $j = [1,2,\ldots,12]$ indicates the joint number;
- $x_i^c(t)$ is the ith story relative displacement (to the ground) at time t for the controlled case;
- $x_i^{\max}$ is the ith story maximum relative displacement (to the ground) for the uncontrolled case;
- $d_i^c(t)$ is the $[i^{\text{th}} - (i^{\text{th}} - 1)]$ story drift at time t for the controlled case;
- h_i is the ith story height, which is 4.5 and 0.45 m for full-scale and 1/10-scale models, respectively;
- $\rho_i^{\max} = \max_t \frac{|d_i(t)|}{h_i}$ is the ith maximum interstory drift ratio for the uncontrolled case. ASCE7-10 recommends ρ should be in the range $0 < \rho < 0.025$ for structures that have up to four stories;
- $\ddot{x}_i^c(t)$ is the ith story absolute acceleration at time t for the controlled case;
- $\ddot{x}_i^{\max}$ is the ith story maximum absolute acceleration for the uncontrolled case;
- m_i is the ith story seismic mass, which is 3534 and 55 kg for full-scale and 1/10-scale models, respectively;
- $F_b^{\max}$ is the maximum base shear for the uncontrolled case;
- $\sigma_j^c(t)$ is the jth joint reinforcement skin stress (von Mises) at time t for the controlled case;
- $\sigma^{\max}$ is the reinforcement skin maximum stress (von Mises) among all joints for the uncontrolled case. From material characterization, the SMP-aramid reinforcement skin has a ultimate tensile stress of 107 MPa at a strain of 1.9%.

In Equations (5)–(13), the norm $\| * \|$ for all metrics is computed through Equation (14):

$$\| * \| = \sqrt{\frac{1}{t_f} \int_0^{t_f} [*]^2 dt}, \tag{14}$$

where t_f is the total time. The values $\|x\|$, $\|\rho\|$, $\|\ddot{x}\|$, $\|F_b\|$, and $\|\sigma\|$ are the normed relative displacement, interstory drift ratio, absolute acceleration, base shear, and reinforcement skin stress for the uncontrolled structure.

T A B L E 2 1/10-Scale model (simulation): Uncontrolled peak response (25°C)

Eearthquake		El Centro	Kobe	Chichi	Kocaeli
$x^{\max}$ (mm)	1S	5.11	3.40	2.03	3.23
	2S	14.0	9.14	5.75	8.89
	3S	19.9	13.5	8.60	12.6
$d^{\max}$ (mm)	1S&2S	9.02	6.02	3.82	5.72
	2S&3S	6.42	4.41	2.97	4.32
$\rho^{\max}$	1S&2S	0.020	0.013	0.0085	0.013
	2S&3S	0.014	0.0098	0.0066	0.0096
$\ddot{x}^{\max}$ (g)	1S	0.455	0.477	0.244	0.339
	2S	0.813	0.545	0.340	0.502
	3S	0.838	0.643	0.421	0.622
$F_{\mathrm{b}}^{\max}$ (kN)		0.99	0.65	0.47	0.60
$\sigma^{\max}$ (MPa)		36.4	24.9	16.2	23.4
$\|x\|$ (mm)	1S	0.97	1.04	0.35	0.91
	2S	2.83	2.97	1.02	2.62
	3S	4.15	4.32	1.49	3.81
$\|d\|$ (mm)	1S&2S	1.86	1.93	0.67	1.71
	2S&3S	1.34	1.38	0.48	1.20
$\|\rho\|$	1S&2S	0.0041	0.0043	0.0015	0.0038
	2S&3S	0.0030	0.0031	0.0011	0.0027
$\|\ddot{x}\|$ (g)	1S	0.067	0.087	0.025	0.067
	2S	0.125	0.139	0.046	0.114
	3S	0.179	0.185	0.064	0.158
F_{b} (kN)		0.18	0.19	0.065	0.17
σ (MPa)		8.23	9.00	3.86	7.55

3.4.2 | Control performance

Table 2 gives metrics related to peak (maximum over time) and normed response for the uncontrolled case (25°C).

Table 3 gives all control criteria evaluated for the joints actuated to the transition temperature. For simplicity, in this analysis, a constant thermal load is applied to increase the joint temperature in discrete steps. Control time delays due to thermal actuation are not considered because the joints are assumed to be actuated at a prescribed temperature when the structure is excited. However, time delay due to thermal actuation is considered in Section 5 for seismic response control simulations on the full-scale model.

Generally, acceleration and base shear reduce significantly when the joints are actuated to the transition temperature compared with the uncontrolled case. Top-story (3S) minimum and maximum acceleration reductions are 23% under Kocaeli earthquake and 62% under El Centro earthquake, respectively. Peak displacement and interstory drift ratio under El Centro earthquake also decrease significantly by 42% and 41%, respectively. However, for the other seismic loadings, there is no significant reduction of displacement and interstory drift ratio, which increase in some cases. The same applies to the stress in the reinforcement skin. Except under El Centro earthquake, the reinforcement skin is subjected to higher stress when the structure is controlled. This is expected because the joint core stiffness decreases upon heating and thus the reinforcement skin takes most of the stress. In some cases, joint stiffness reduction may also result in an increase of the structure deformation (story displacement) and interstory drift. That being said, interstory drift ratio and reinforcement skin stress are lower than required limits in the worst case ($0 < \rho < 0.025$, $\sigma < 107$ MPa). In some cases, for example under Kocaeli earthquakes, the joint stiffness reduction causes the structure frequency to shift into a high energy frequency range of the seismic loading. While peak and normed accelerations of all stories reduce owing to the increase of structural damping caused by joint thermal actuation (viscoelastic effects), top-story peak and normed displacement increase significantly by up to 68% and 43%, respectively. A better performance is obtained when the joints are actuated to 60°C. At

TABLE 3 1/10-Scale model (simulation): Control performance through adaptive structural joints

Eearthquake		El Centro65°C	Kobe65°C	Chichi65°C	Kocaeli60°C
J_1 (peak displacement)	1S	0.42	0.66	0.72	0.97
	2S	0.53	0.84	0.91	1.10
	3S	0.58	0.90	0.97	1.16
J_2 (peak drift ratio)	1S&2S	0.59	0.93	1.00	1.17
	2S&3S	0.65	1.14	1.12	1.16
J_3 (peak acceleration)	1S	0.69	0.83	0.93	0.86
	2S	0.55	0.69	0.81	0.83
	3S	0.38	0.75	0.73	0.77
J_4 (peak base shear)		0.35	0.50	0.59	0.86
J_5 (peak skin stress)		0.64	0.99	1.02	1.19
J_{1n} (normed displacement)	1S	0.53	0.55	0.83	1.04
	2S	0.65	0.66	1.01	1.15
	3S	0.70	0.70	1.08	1.19
J_{2n} (normed drift ratio)	1S&2S	0.72	0.73	1.12	1.22
	2S&3S	0.81	0.81	1.22	1.27
J_{3n} (normed acceleration)	1S	0.82	0.66	0.85	0.94
	2S	0.50	0.54	0.68	0.90
	3S	0.47	0.47	0.67	0.90
J_{4n} (normed base shear)		0.43	0.43	0.65	0.90
J_{5n} (normed skin stress)		0.99	0.95	1.71	1.28

this temperature, peak and normed accelerations are minimized, and the top-story displacement increases marginally by 16%.

Top-story uncontrolled versus controlled response time history together with peak acceleration and interstory drift ratio profiles over the structure height are shown in Figure 5. It is clear from the time history response that a medium-to-high reduction of peak acceleration is obtained depending on the type of seismic loading. Except for El Centro earthquake, maximum relative displacement and interstory drift ratio increase. This is expected because the structure becomes more flexible owing to the stiffness reduction caused by thermal actuation of the joints. In addition, in some cases such as under Kocaeli and Chichi earthquakes, the joint stiffness reduction results in the structure frequency shifting into a high energy frequency range of the seismic loading, which increases displacement and interstory drift responses. Further considerations on this aspect are given in Section 3.5.

3.5 | Result interpretation through response spectra

In Section 3.4, it has been observed that control performance through thermal actuation of variable stiffness and damping joints varies depending on the type of seismic loading. To gain a deeper insight into the performance of this new control strategy, it is useful to employ a response spectrum. Assuming the structure can be idealized as a single-degree-of-freedom system with a known damping ratio and natural frequency, the peak response can be estimated from the ground response spectrum. In this work, a response spectrum is employed to appreciate the effect of frequency shift caused by thermal actuation of the adaptive joints. Acceleration and displacement response spectra, computed through software *SeismoSignal*, are shown in Figure 6A and Figure 6B, respectively. The first two modes are considered. The grey regions indicate the frequency shift for first and second modes caused by joint thermal actuation from ambient 25°C to transition temperature 65°C. The structure damping ratio is set to 2.6% as obtained from experimental testing at ambient temperature (Section 4.3).

The effect of material damping variation due to viscoelastic effects is neglected. As observed from numerical simulations, the structure damping ratio varies from 2.6% to 9.5% owing to the increase of material damping through thermal
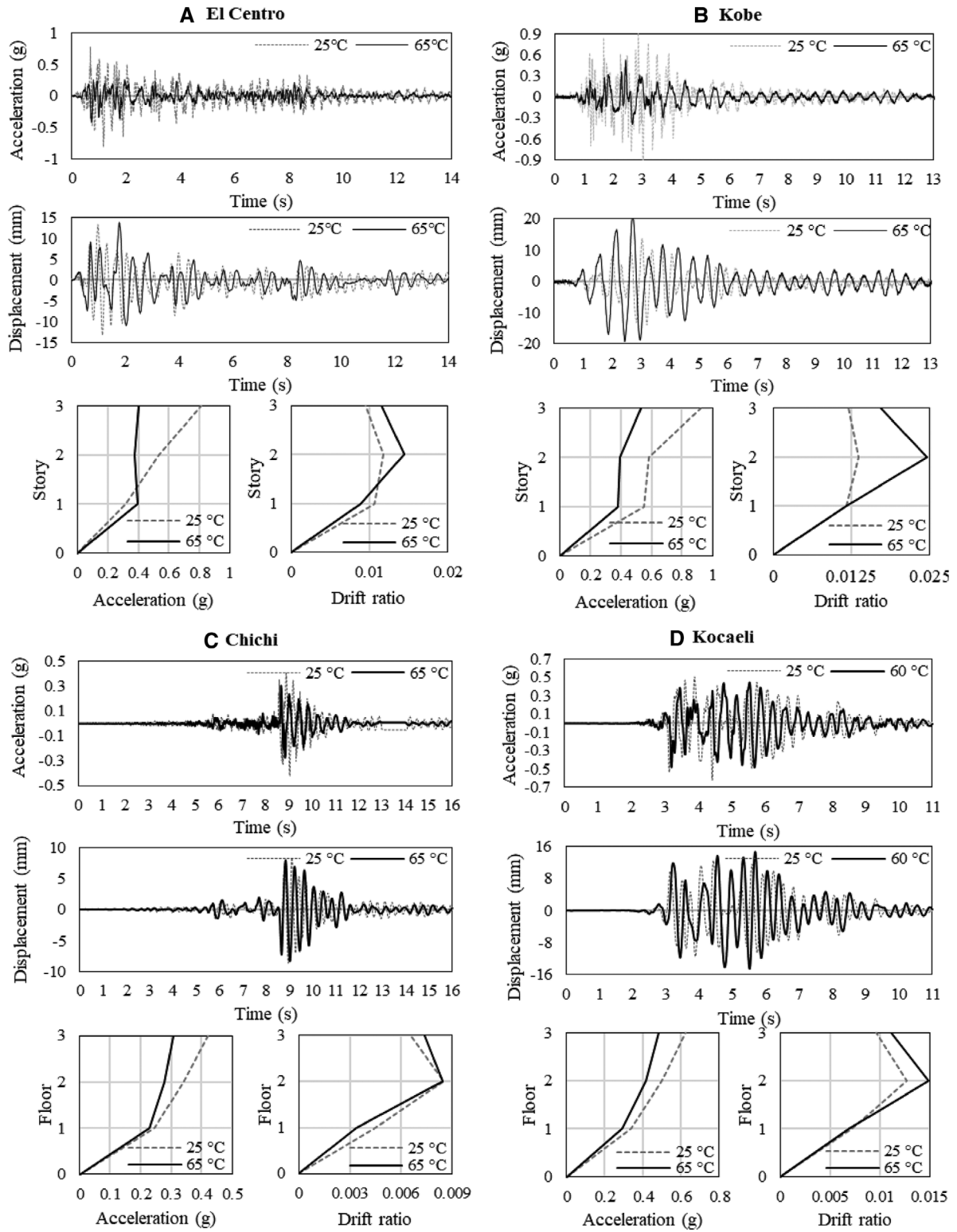
FIGURE 5 1/10-Scale model (simulation) under (A) El-Centro, (B) Kobe, (C) Chichi, and (D) Kocaeli earthquakes. Top-story uncontrolled (25°C) versus controlled (65°C) acceleration and displacement response time history; peak acceleration, and interstory drift ratio profiles
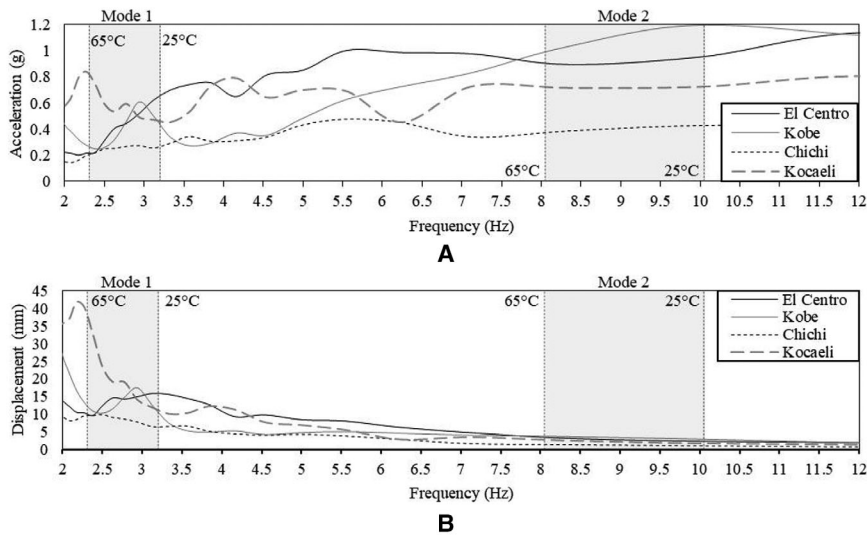
FIGURE 6 Acceleration (A) and displacement (B) spectra (2.6% damping ratio)

actuation of the joints from ambient to transition temperature. For this reason, acceleration and displacement responses obtained through simulation (Section 3.4) are generally smaller than those reported in the spectra (Section 3.4). As can be seen from the spectra, frequency shift helps to reduce the structure response under some seismic loadings, for example, El Centro and Chichi. However, in other cases, for example, Kobe and Kocaeli, the effect of frequency shift is not beneficial because it increases the structure response.

Under El Centro earthquake, acceleration and displacement response decrease significantly through joint thermal actuation. Frequency shift and increase of damping contribute to reducing the top-story acceleration and displacement by up to 62% and 42%, respectively (Table 3). This agrees with the estimation given by acceleration and displacement response spectra in Figure 6. Generally, the increase of structure damping ratio through joint thermal actuation contributes to reducing the increase of displacement that would occur owing to joint stiffness reduction as shown by the displacement spectra in Figure 6B. For example, the displacement response would remain practically constant for Kobe and increase moderately for Chichi, according to the response spectrum. However, owing to the increase of structure damping ratio caused by joint thermal actuation, the top-story displacement is reduced by 10% under Kobe and by 3% under Chichi (Table 3). As previously observed, under Kocaeli earthquake, joint stiffness reduction causes the structure frequency to shift into a high energy frequency range of the excitation. From the spectra in Figure 6, first mode acceleration and displacement responses would increase dramatically when the joints reach the transition temperature. However, from time history analysis (Table 3, Figure 5D), while the top-story displacement increases by 68%, the acceleration is reduced by up to 20% owing to the increase of structural damping. Under Kocaeli earthquake, better control performance is obtained when the joint control temperature is set to 60°C to avoid the large increase of acceleration and displacement that occurs at 65°C due to the effect of frequency shift.

4 | EXPERIMENTAL TESTING ON A 1/10-SCALE THREE-STORY FRAME

4.1 | Experimental setup

Figure 7 shows a schematic view of the experimental setup. Dimensions and main characteristics of the structural model have been given in Section 3.1. The frame is subjected to one-dimensional ground motion generated by a linear actuator (T60 actuator and BGM09 belt gear from *Thomson*, AKM42E-ANCNC-00 BLDC Motor from National Instruments), which is connected directly to a shaking table. A real-time target machine (NI cRIO-9038, National Instruments) is employed to control the linear actuator motion, measure the joint temperature, and modulate the power supply for thermal actuation of the joints. A data acquisition system (cDAC-9178, National Instruments) is employed to monitor the structure response, which is measured through accelerometers, a draw-wire sensor, three laser sensors, and four strain gauge sensors. Ground acceleration and displacement are measured by an accelerometer (BDK3 from seika.de) and a draw-wire displacement sensor (500-FD60 from Altheris sensors & controls), which are located on the left side of the shaking table. Three additional accelerometers are installed in the middle of the left-side beams to measure the *x*-axis acceleration component for each
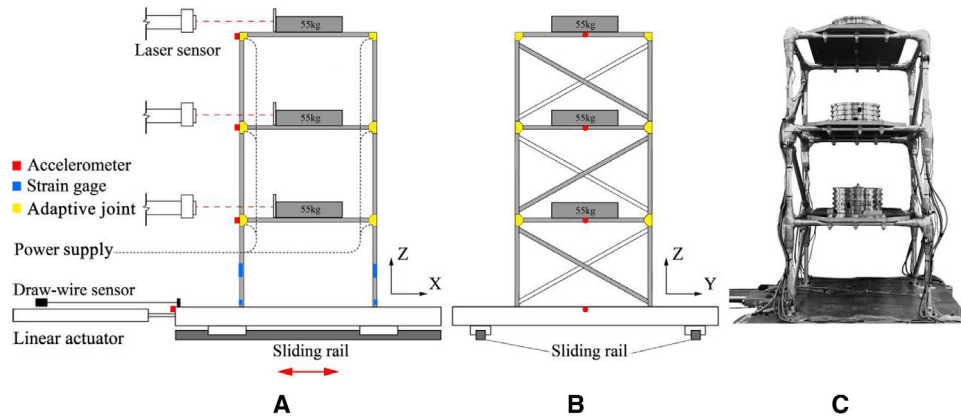
FIGURE 7 Experimental setup: front (A) and side (B) view, (C) three-story adaptive frame prototype

story. The accelerometers are indicated by red square markers in Figure 7A,B. The story displacements are measured by three laser sensors (M5L-200 from MEL Mikroelektronik GmbH). Axial and bending stresses of two of the first story columns are monitored through strain gauge sensors, which are indicated by blue markers in Figure 7A. To monitor axial stress, two strain gauge rosettes (1-XY33-3/350, HBM) are installed in a full-bridge configuration and placed in the middle of the column, while for bending stress two strain gauges (PEL-10-11, Tokyo Sokki Kenkyujo) are installed in a quarter-bridge configuration and placed toward the support end of the column. Figure 7C shows a photo of the adaptive frame prototype.

4.2 | Thermal actuation system

Stiffness and damping characteristics of 12 adaptive joints are controlled independently through a proportional–integral–derivative controller (PID). As shown in Figure 1, a resistive heating wire is embedded in the core of each joint. The length of the embedded heating wire is approximately 1.8 m for joints that connect three elements and 2.2 m for joints that connect four elements. Figure 8A shows 12 solid-state relays (DC60S5, Crydom), which are controlled by the real-time controller to modulate the power supply to each heating wire independently. A resistance temperature detector (RTD) (F2020-100-A, Omega) is installed on each heating wire to control the thermal flux. Two power supplies (230 V/12 VDC, 350 W, Schloss) are employed for thermal actuation. A thermocouple is installed on the surface of each joint to monitor the temperature that is recorded through a multichannel data logger (Squirrel 2040, Grant). An infrared thermometer is employed to verify thermocouple measurements as shown in Figure 8B. To minimize interaction with field temperature, a layer of insulating material (bubble wrap with double-sided heat-reflective coating, GAMMA) is applied on each joint as shown in Figure 8C.
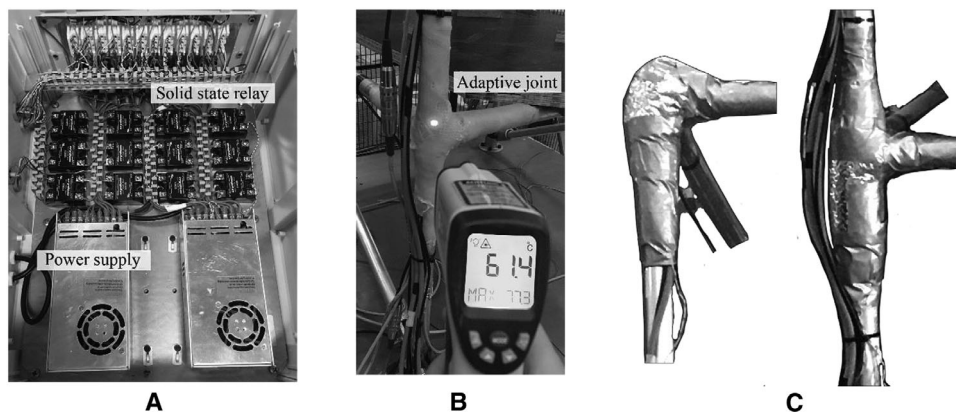

FIGURE 8 (A) Power supply and solid-state relays; (B) temperature measurement through thermocouple and infrared thermometer; (C) adaptive joints covered with insulation material

As thermal actuation is carried out through resistive heating, a preliminary estimate of the energy required to actuate a joint is

$$Q_1 = cm\Delta T, \tag{15}$$

where c is the specific heat capacity of the joint core material and ΔT is the required temperature increment from ambient to transition temperature. Assuming the specific heat capacity for the SMP joint core is 1.4 kJ/(kg°C), and considering that the average joint mass for the 1/10-scale prototype is 40 g, from Equation 15 the required energy is 2.24 kJ. The energy generated through resistive heating is

$$Q_2 = \frac{U^2}{R}t = Pt, \tag{16}$$

where U is the power supply voltage, t is the heating time, R and $P = \frac{U^2}{R}$ are the heating element resistance and power rating, respectively. If heat transfer time and energy dissipation are ignored, let $Q_1 = Q_2$. Considering a heating wire with an average length of 2 m, the resistance R has been measured at 2.84 ohm. Given a 350 W 12 VDC power supply, as used in this experimental setup, the average heating wire power rate is 50 W. From Equation (16), the average time to actuate the joint from ambient to transition temperature is 45 s. The actuation time could be significantly reduced by increasing the heating wire power rate. For example, by using a 500 W 36 VDC power supply for each joint the average actuation time would be reduced to 5 s. However, this hardware architecture requires a more sophisticated temperature control system to prevent potential damage caused by burns. For this reason, sufficient time has been allowed so that the joint temperature stabilizes to the set value before application of the base excitation. As done for the 1/10-scale model simulation (Section 3.4), the effect of control time delays due to joint thermal actuation is not evaluated through testing. However, time delay due to thermal actuation is considered in Section 5 for seismic response control simulations on the full-scale model.

4.3 | Frequency shift and damping ratio variation measurement

Frequency shift and damping variation caused by thermal actuation of the joints are measured through free vibration tests. As carried out for numerical simulations (Section 3.2), the joints are actuated from ambient to transition temperature in discrete steps. A 20 mm base displacement is applied through the shake table. The free vibration is recorded through the accelerometers (Section 2.1) for a period of 100 s. For each temperature, the measurement is repeated four times. The recorded acceleration is averaged over the four measurements. Natural frequency and frequency shift for first and second modes are given in Table 4. The modal frequencies are obtained through fast Fourier transforms (FFTs) of the recorded acceleration. First- and second-mode frequency shifts from ambient (25°C) to transition temperature (65°C) are $S_{\omega 1}^e = 37.1\%$ (from 3.34 to 2.1 Hz) and $S_{\omega 2}^e = 31.2\%$ (from 10.96 to 7.54 Hz), respectively. The superscript e stands for "experimental." At 25°C, the measured frequency (3.34 Hz) is marginally higher than the frequency obtained from modal analysis (3.2 Hz). However, when the joints are actuated above 40°C, all measured frequencies are lower and thus all frequency shifts are larger than the corresponding values obtained from simulation. The maximum discrepancy between simulation and experimental results has been recorded for both first and second modes at 50°C (21.3% and 17.2% experimental vs. 3.4% and 3.1% as obtained from simulation). Referring to Figure 2, at approximately 50°C the joint core material enters the viscoelastic region in which storage modulus and material damping vary significantly. Joint temperature control is based on feedback from thermocouples installed on the joint surface that generally is at a lower temperature compared with the core. This leads to a more pronounced stiffness reduction of the joints than expected, which results in larger structure frequency shifts measured experimentally compared with numerical predictions. Such discrepancy reaches the

TABLE 4 1/10-Scale prototype: Frequency and damping variation for first and second modes

	25°C	40°C	45°C	50°C	55°C	60°C	65°C
ω_1^e (Hz)	3.34	2.88	2.77	2.57	2.43	2.32	2.10
ω_2^e (Hz)	10.96	9.63	9.32	9.08	8.84	8.23	7.54
$S_{\omega 1}^e$ (%)	–	13.8	17.1	23.1	27.2	30.5	37.1
$S_{\omega 2}^e$ (%)	–	12.1	15.0	17.2	19.3	24.9	31.2
ζ^e (%)	2.6	4.4	5.3	6.4	8.0	9.4	11.3

maximum as the joints are actuated from ambient to approximately 50°C, and then reduces as the temperature reaches the range 60°C–72°C in which the storage modulus is less sensitive to temperature variation.

The logarithmic decrement method (Equation 3) is applied to compute the damping ratio variation, which is given in Table 4. The free vibration peaks of the top-story displacement are measured with a laser sensor. Resampling, smoothing, and filtering have been carried out through software *NI DIAdem 2019 SP1*. In good accordance with numerical predictions, the increase of material damping due to viscoelastic effects caused by thermal actuation of the joints results in a significant 4.3-fold increase (3.6-fold from simulation) of the structure damping ratio from 2.6% at ambient temperature to 11.3% at transition temperature. Generally, the damping ratio measured experimentally is higher than that obtained through simulation. Similar to what has been observed for the frequency shift, such discrepancy reaches the maximum at 50°C–55°C and then reduces as the temperature further increases. Since the joint core temperature is generally higher than the surface temperature measured by thermocouples, a higher damping ratio is measured experimentally compared with numerical predictions.

4.4 | Experimental testing of semi-active response control through adaptive structural joints

Simulation results (Section 3.4) on seismic response control of the 1/10-scale three-story frame model are benchmarked through experimental testing. The dynamic response is recorded as the joints are actuated from ambient 25°C to transition temperature 65°C in discrete steps. The joint temperature is set through PID control using feedback from thermocouples that are installed on the surface of each joint. Sufficient time is given so that the joint temperature stabilizes to the set value before application of the base excitation.

4.4.1 | Response control under harmonic load

Control performance is first evaluated under a sinusoidal ground motion. The base excitation has a frequency of 3.0 Hz, an amplitude of 1 mm, and it is applied for a period of 10 s. Note that the first modal frequency measured through free vibration tests is 3.34 Hz. However, it was found through testing that the first mode is excited when the base excitation frequency is set to 3.0 Hz. This difference is likely to be attributed to some degree of looseness in the connections between diagonal bracings and columns, between the plates that house the steel weights and story beams, and in the connections between the frame structure and the shaking table.

Figure 9 shows top-story maximum acceleration and displacement responses for the uncontrolled case (25°C) as well as when for the joints actuated to 50°C and 65°C. Top-story acceleration and displacement reduce by up to 76% (from 0.324*g*
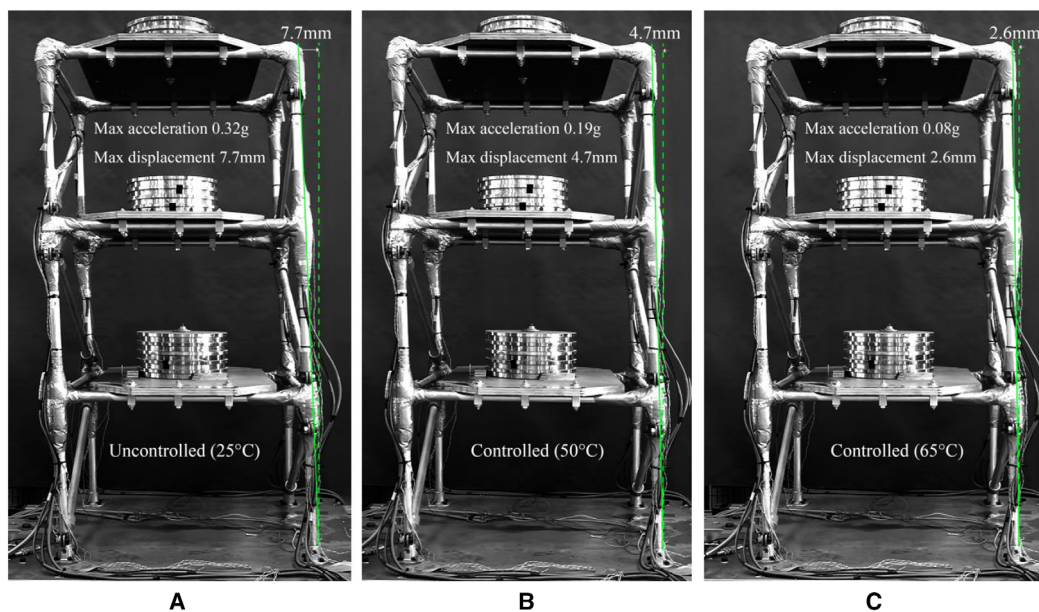

FIGURE 9   1/10-Scale prototype top-story displacement under sinusoidal base excitation: (A) uncontrolled (25°C), joints actuated to (B) 50°C and (C) 65°C
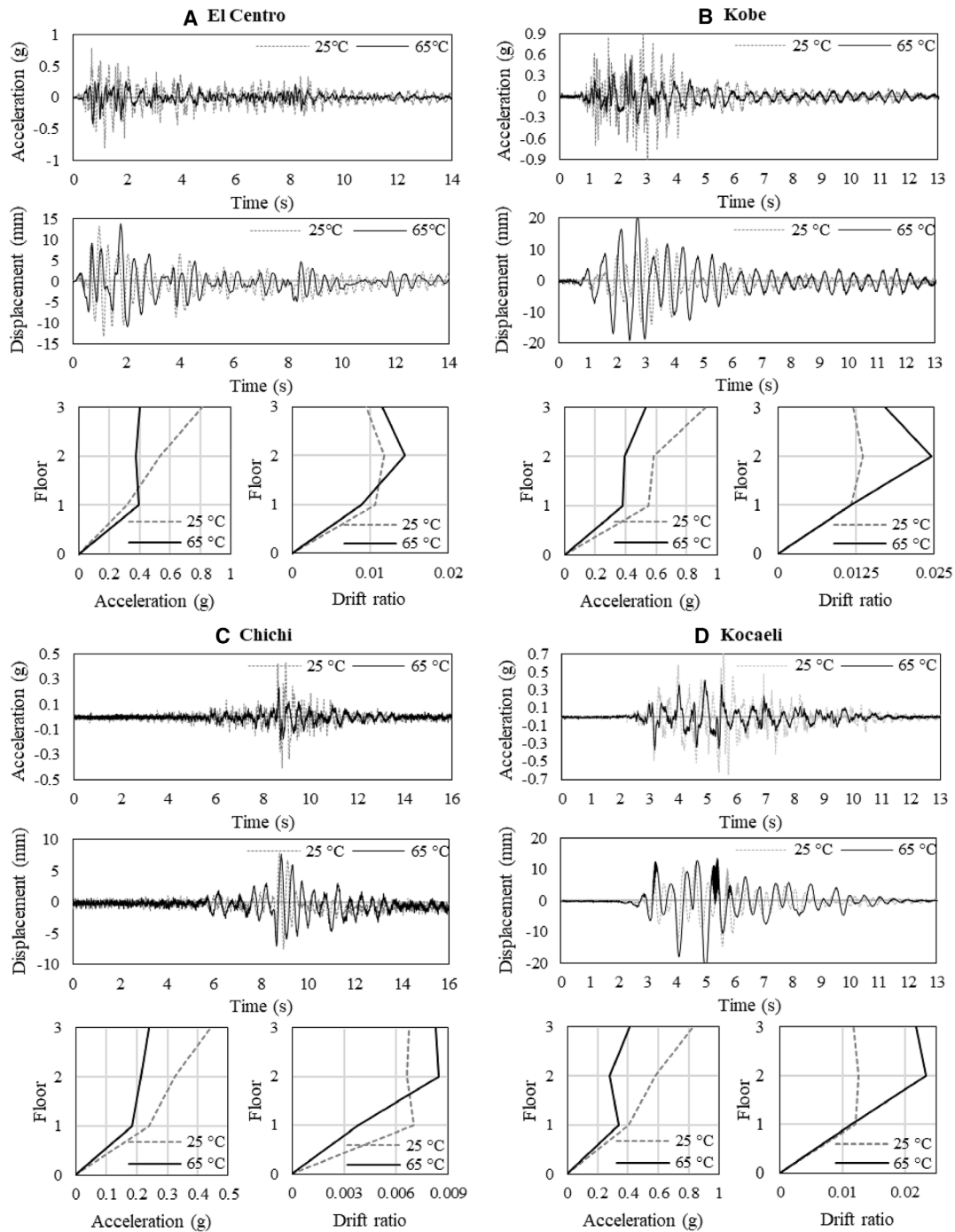
FIGURE 10 1/10-Scale prototype under (A) El Centro, (B) Kobe, (C) Chichi, and (D) Kocaeli earthquakes. Top-story uncontrolled (25°C) versus controlled (65°C) acceleration and displacement response time history; peak acceleration and interstory drift ratio profiles

to 0.079g) and 66% (from 7.7 mm to 2.63 mm), respectively, when the joints are actuated to the transition temperature. A video demonstration has been included as supplementary material (see Supporting Information) and is available online https://vimeo.com/495264243.

4.4.2 | Response control under seismic loading, simulation versus experimental

Dynamic response and control performance under the same seismic loadings defined in Section 3.3 are measured through shake-table tests and compared with simulation results (Section 3.4). The ground acceleration for all seismic loadings

TABLE 5   1/10-Scale model control performance, simulation (S) versus experimental (E)

Eearthquake		El Centro		Kobe		Chichi		Kocaeli	
		S	E	S	E	S	E	S(60°C)	E(65°C)
J_1 (peak displacement)	1S	0.42	0.83	0.66	1.00	0.72	0.55	0.97	0.95
	2S	0.53	0.95	0.84	1.45	0.91	0.91	1.10	1.51
	3S	0.58	1.03	0.90	1.56	0.97	0.99	1.16	1.57
J_2 (peak drift ratio)	1S&2S	0.59	1.22	0.93	1.81	1.00	1.27	1.17	1.99
	2S&3S	0.65	1.20	1.14	1.41	1.12	1.23	1.16	1.21
J_3 (peak acceleration)	1S	0.69	1.26	0.83	0.69	0.93	0.60	0.86	0.83
	2S	0.55	0.70	0.69	0.68	0.81	0.43	0.83	0.49
	3S	0.38	0.50	0.75	0.57	0.73	0.54	0.77	0.50
J_4 (peak base shear)		0.35	0.53	0.50	0.52	0.59	0.49	0.86	0.65
J_{1n} (normed displacement)	1S	0.53	0.71	0.55	1.12	0.83	1.05	1.04	0.84
	2S	0.65	0.87	0.66	1.51	1.01	1.05	1.15	1.27
	3S	0.70	0.96	0.70	1.65	1.08	1.23	1.19	1.42
J_{2n} (normed drift ratio)	1S&2S	0.72	1.11	0.73	1.90	1.12	1.60	1.22	3.09
	2S&3S	0.81	1.11	0.81	1.69	1.22	1.32	1.27	2.68
J_{3n} (normed acceleration)	1S	0.82	0.93	0.66	0.63	0.85	0.59	0.94	0.72
	2S	0.50	0.61	0.54	0.63	0.68	0.54	0.90	0.63
	3S	0.47	0.50	0.47	0.55	0.67	0.60	0.90	0.60
J_{4n} (normed base shear)		0.43	0.59	0.43	0.60	0.65	0.59	0.90	0.57

has been resampled through *SeismoSignal* with a time step of 0.005 s, which gives a maximum average error on acceleration of 5.8% for El Centro seismic loading. This is also the time step between two consecutive commands that are sent to the linear actuator to generate the required ground motion. Top-story absolute acceleration and relative displacement responses obtained from experimental testing are given in Figure 10A–D.

Generally, acceleration and displacement response obtained through simulation are in good accordance with experimental values (compare Figures 5 and 10). Measured and simulated controlled responses differ the most under Kocaeli earthquake. The frequency shift measured when the joints are actuated to the transition temperature is greater than that obtained through simulation ($S_{\omega 1}^e$ = 37.1% vs. $S_{\omega 1}^s$ =27.7%). This avoids overlapping with the high energy frequency component range of the excitation, and together with a greater damping ratio (ζ^e =11.3% vs. ζ^s =9.5%), results in a better control performance when the joints are actuated to the transition temperature instead of 60°C as observed through simulation. For clarity, a side-by-side comparison of the time history response under each earthquake obtained through simulations and experimental studies has been included as supplementary material (see Supporting Information).

Table 5 gives control performance indicators between simulation and experimental testing with regard to top-story acceleration and displacement as well as interstory drift. The structure damping ratio is greater than that predicted through simulation as observed in Section 4.3 (compare Tables 1 and 4). For this reason, the measured acceleration response reduction is greater (twice as much on average) compared with that obtained through simulation. However, as the stiffness reduction caused by thermal actuation of the joints is more pronounced than that predicted through analysis, the measured displacement and interstory drift are greater than those predicted through simulation. The maximum interstory drift (11.1 mm) occurs between first and second story under Kobe earthquake for the controlled state (J_2 = 1.81 in Table 4). Considering the floor height is 450 mm, the maximum interstory drift ratio is 11.1/450 = 0.0246, which is lower than 0.025 as required by ASCE7-10. Although differences exist between numerical and experimental results, shake-table tests have confirmed that the control strategy proposed in this work based on thermal actuation of variable stiffness and damping joints is effective to reduce story acceleration and base shear in the range 43%–50% and 35%–51%, respectively.

TABLE 6   Scale factors of selected structure parameters

Parameter	Symbol	Scale factor	For $\lambda = 10$
Length	λ_L	λ	10
Young's modulus	λ_E	1	1
Volume	λ_V	λ^3	1000
Self-weight	λ_{sw}	λ^3	1000
Mass floor	λ_m	λ^2	100
Acceleration	λ_a	1	1
Time	λ_T	$\lambda^{1/2}$	3.16
Frequency	λ_ω	$\lambda^{-1/2}$	0.316
Strain	λ_ε	1	1
Stress	λ_σ	1	1

5 | NUMERICAL STUDY ON A FULL-SCALE THREE-STORY FRAME

5.1 | Full-scale numerical model

The conclusions reached through numerical and experimental testing on the 1/10-scale structural model (Sections 3 and 4) are generalized through simulation on the full-scale model. The full-scale model is derived by scaling up the 1/10-scale model based on Cauchy and Froude similitude laws.[37] Table 6 gives the scaling factors of selected structure parameters. All factors are related to the geometric scaling $\lambda = 10$. The dimensions of the full-scale model are $13.25 \times 6.50 \times 6.50$ m. The aluminum tube elements have a diameter of 250 mm and a wall thickness of 25 mm.

The scaling factors adopted in this study are chosen to keep material properties unchanged. Referring to modal analysis for the 1/10-scale model (Table 1), the first modal frequency at 25°C for the full-scale model should be 3.2 Hz $\cdot \lambda^{-1/2} = 1.01$ Hz. However, a preliminary modal analysis shows that the first modal frequency of the full-scale model at 25°C is 0.864 Hz. In order to adjust the natural frequencies to the required values, the dead load applied on each floor of the full-scale model is reduced from 150 kg/m^2 (as applied to the 1/10-scale model) to approximately 100 kg/m^2.

5.2 | Frequency shift and damping ratio variation through joint thermal actuation

Similar to Section 3.2, frequency and damping variation caused by joint thermal actuation are computed through modal analysis and free vibration test simulations through full-transient analysis, respectively. The joints are actuated from ambient (25°C) to transition temperature (65°C) in discrete steps through a time-constant thermal load. The structural damping ratio is computed through the logarithmic decrement of the displacement peak for a time period of 10 s. Similar to the 1/10-scale model, because at ambient temperature the joint core material is elastic, the structure damping ratio at 25°C is set to 2.6% as measured from experimental testing (Section 3.2).

Results are given in Table 7. First and second modes frequency shift of the full-scale model are in very good accordance with those of the 1/10-scale model (compare with Table 1). For example, at 65°C, first and second mode frequency shift for the full-scale model are $S_{\omega 1} = 27.5\%$ and $S_{\omega 2} = 23.0\%$ and those for the 1/10-scale model are $S_{\omega 1}^S = 27.7\%$ and $S_{\omega 1}^S = 23.3\%$. Similarly, the damping ratios of full-scale and 1/10-scale models are in good accordance. The largest discrepancy is

TABLE 7   Full-scale model: Frequency shift and modal damping of first and second modes from simulation

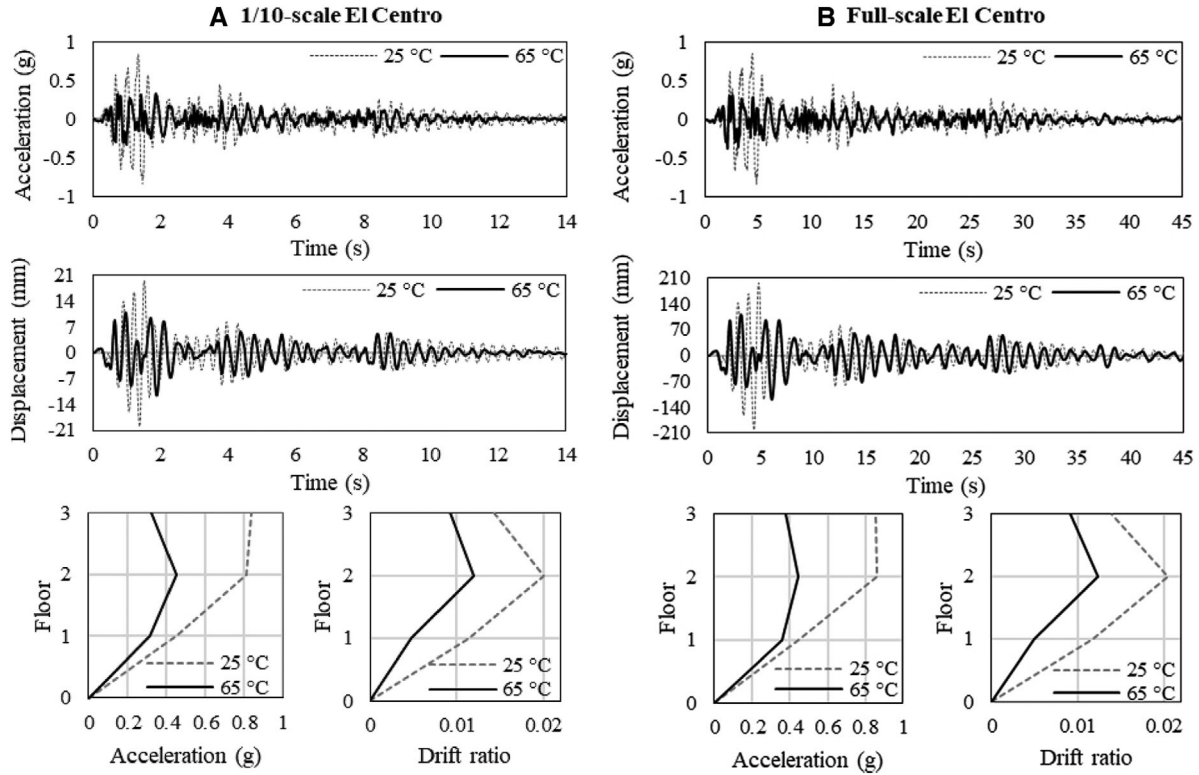|	25°C	40°C	45°C	50°C	55°C	60°C	65°C
ω_1 (Hz)	1.01	1.00	1.00	0.98	0.91	0.82	0.73
ω_2 (Hz)	3.32	3.28	3.27	3.22	3.03	2.78	2.56
$S_{\omega 1}$ (%)	–	1.2	1.5	3.4	10.0	19.0	27.5
$S_{\omega 2}$ (%)	–	1.1	1.4	3.0	8.7	16.2	23.0
ζ (%)	2.6	2.6	2.7	3.6	5.2	7.8	8.1

FIGURE 11 (A) 1/10-Scale versus (B) full-scale model under El Centro earthquake: top-story uncontrolled (25°C) and controlled (65°C) response time history; peak acceleration and interstory drift ratio profiles

observed at 65°C, as the damping ratio of the 1/10-scale model ($\zeta^s = 9.5\%$) is 1.4% higher than that of the full-scaled model ($\zeta = 8.1\%$).

5.3 | Semi-active seismic response control through adaptive structural joints, full scale versus 1/10-scale

The uncontrolled response and control performance of 1/10-scale and full-scale models are first compared under El Centro 1940 earthquake. In this simulation, joint actuation is simulated through a time-constant thermal load. Top-story absolute acceleration and relative displacement time histories for the uncontrolled (25°C) and controlled case (65°C), as well as peak acceleration and interstory drift ratio profiles are shown in Figure 11. Control performance is given in Table 8. Both uncontrolled and control performance of 1/10-scale and full-scale models are in good accordance. For example, top-story peak acceleration is reduced by 55.9% (from 0.85g to 0.38g) for the full-scale model and by 61.6% (from 0.84g to 0.32g) for the 1/10-scale model. The larger reduction for the 1/10-scale model is caused by a higher damping ratio at 65°C (Table 7). Top-story displacement reductions are 41.4% (from 201 to 118 mm) and 41.7% (from 19.9 to 11.6 mm) for the full-scale and 1/10-scale models, respectively.

As expected, from laws of similitude, acceleration and displacement scale factors between full-scale and 1/10-scale models are approximately $\lambda_a = 1$ and $\lambda_L = 10$, respectively. For the base shear (Equations 10 and 11), the scale factor should be $\lambda_{bs} = \lambda_a \lambda_m$, where $\lambda_a = 1$ is the acceleration factor and $\lambda_m = DL_f \lambda^2$ is the floor mass factor that scales with the square of the floor area. The dead load has been scaled by $DL_f = \frac{100(\text{kg/m}^2)}{150(\text{kg/m}^2)} = 0.67$ in order to obtain the expected structural frequency ratio between 1/10-scale and full-scale models (Section 5.1). Hence the base shear scale factor $\lambda_{bs} = \lambda_a\ DL_f\ \lambda_m = 1 \cdot 0.67 \cdot 10^2 = 67$. Simulation results are in good accordance with the prediction through dimensional analysis. The peak base shear between full-scale and 1/10-scale models is 67.5/0.99 = 68. A similar scale factor of 63 is obtained for the normed base shear.

TABLE 8   1/10-Scale model versus full-scale model: Uncontrolled response and control performance

Eearthquake		Uncontrolled (25°C) 1/10-Scale	Full-scale	Controlled (65°C) 1/10-Scale	Full-scale		Evaluation criteria 1/10-Scale	Full-scale
$x^{\max}$ (mm)	1S	5.11	52.7	2.14	22.0	J_1	0.42	0.42
	2S	14.0	143	7.46	77.6		0.53	0.54
	3S	19.9	201	11.6	118		0.58	0.59
$\rho^{\max}$	1S&2S	0.020	0.020	0.012	0.012	J_2	0.59	0.61
	2S&3S	0.014	0.014	0.0093	0.0092		0.65	0.66
$\ddot{x}^{\max}$ (g)	1S	0.455	0.446	0.314	0.360	J_3	0.69	0.81
	2S	0.813	0.858	0.450	0.442		0.55	0.51
	3S	0.838	0.852	0.322	0.375		0.38	0.44
$F_b^{\max}$ (kN)		0.99	67.5	0.35	20.9	J_4	0.35	0.31
$\sigma^{\max}$ (MPa)		36.4	36.7	23.4	22.2	J_5	0.64	0.60
$\|x\|$ (mm)	1S	0.97	9.76	0.52	5.57	J_{1n}	0.53	0.57
	2S	2.83	28.1	1.84	20.0		0.65	0.71
	3S	4.15	40.8	2.89	31.2		0.70	0.76
$\|\rho\|$	1S&2S	0.0041	0.0041	0.0030	0.0032	J_{2n}	0.72	0.79
	2S&3S	0.0030	0.0028	0.0024	0.0026		0.81	0.90
$\|\ddot{x}\|$ (g)	1S	0.067	0.065	0.055	0.057	J_{3n}	0.82	0.87
	2S	0.125	0.123	0.062	0.064		0.50	0.52
	3S	0.179	0.176	0.084	0.088		0.47	0.50
$\|F_b\|$ (kN)		0.18	11.2	0.07	4.75	J_{4n}	0.43	0.43
$\|\sigma\|$ (MPa)		8.23	7.89	8.10	8.29	J_{5n}	0.99	1.05

5.4 | Semi-active seismic response control considering time delay

5.4.1 | Control time delays

In addition to scaling effects, two types of control time delay are considered: (a) the time it takes for detection of the external excitation, (b) the time it takes for thermal actuation of the joints from ambient to transition temperature once the excitation has been detected. For simplicity, the acceleration activation threshold has been set to 100 mm/s^2, which is generally large enough to eliminate interference with ambient vibration. Referring to Section 2.3, joint thermal actuation is activated only after the measured ground acceleration exceeds the set activation threshold.

The time it takes to actuate the joint from ambient (field) to transition temperature depends primarily on the type of SMP joint core material as well as the type of heat transfer technology and activation stimulus adopted (e.g., resistive, magnetic actuation). The SMP material adopted in this study has a transition temperature of 65°C, while the field temperature is assumed to be 25°C. Thermal actuation is assumed to be carried out through resistive heating as done for simulation and testing on the 1/10-scale model. With regard to the full-scale model considered in this section, the joint average mass is approximately 35 kg. Assuming the specific heat capacity for the SMP joint core is 1.4 kJ/(kg°C), from Equation (15) an estimate of the energy required to actuate the joint from ambient (25°C) to transition temperature (65°C) is 1960 kJ. Assuming an appropriate power supply and a heating rate of 5°C/s, five heating elements with a power rate of 50 kW are sufficient to limit the required heating time to 8 s (Equation 16). Note that this is the time it takes to actuate the joints to the transition temperature at which the damping ratio increases the most. However, generally, the effect of frequency shift and increase of damping ratio is significant as the joint core material enters the viscoelastic region (from 50°C), which takes approximately 5 s.

5.4.2 | Uncontrolled versus controlled response considering time delay

Considering time delays due to heating, a time-linear thermal load with a heating rate of 5°C/s from 25°C to 65°C in 8 s is applied to the joint elements of the full-scale model under El Centro and Chichi earthquakes. Top-story absolute
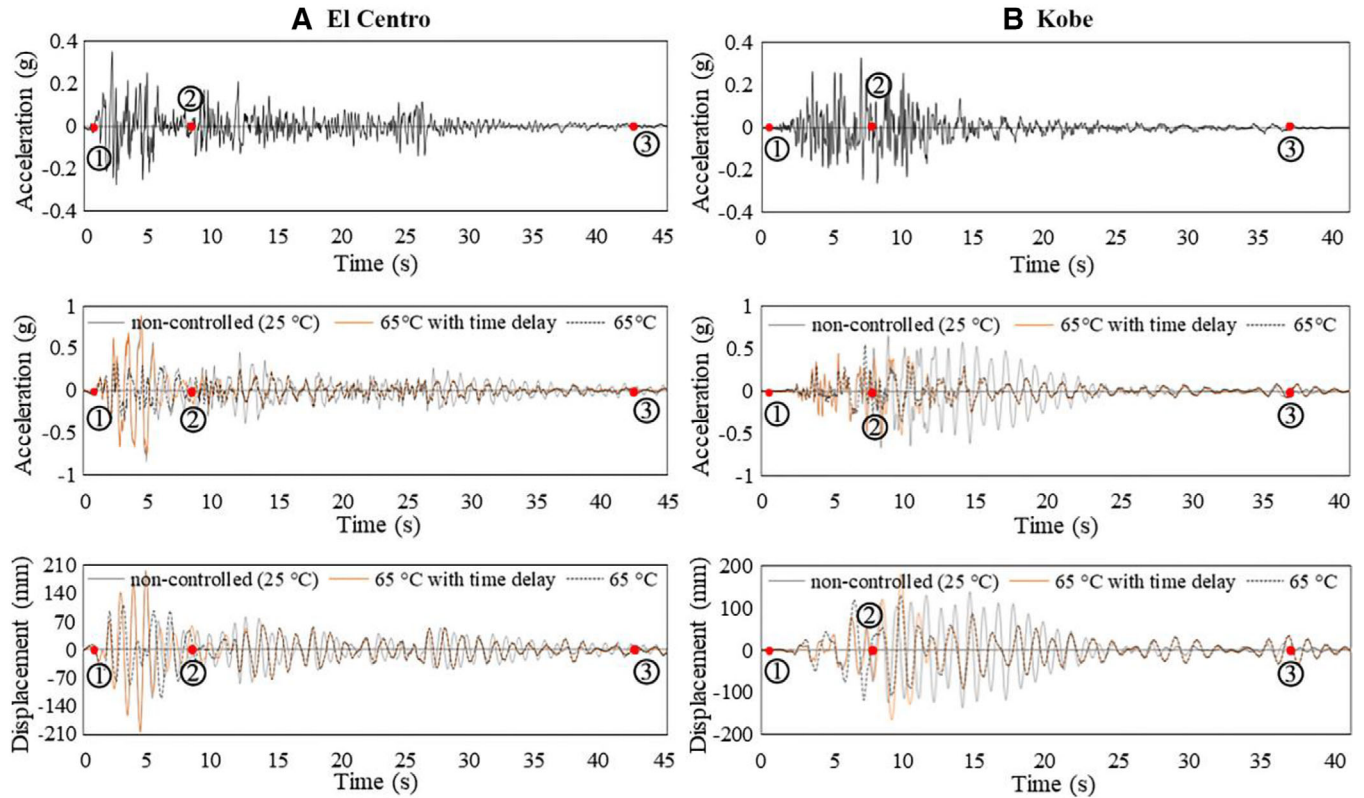
FIGURE 12 Full-scale model under (A) El Centro and (B) Kobe earthquakes: top-story acceleration and displacement response time history

acceleration and relative displacement responses are shown in Figure 12. Points 1, 2, and 3 indicate: 1) activation of joint thermal actuation due to the detection of external excitation when the ground acceleration is greater than the set threshold of 100 mm/s^2; 2) the joint control temperature has reached the transition value; 3) thermal actuation is switched off as the ground acceleration has become smaller than the activation threshold (natural cooling of the joints begins).

Control performance is given in Table 9. The uncontrolled case (25°C) is indicated by a grey curve, while controlled cases with constant and linear thermal load are indicated by a black dash and an orange curve, respectively. Generally, during the first 5 s (25°C to 50°C), as the joint core material has not yet entered the viscoelastic region (Figure 2A), controlled and uncontrolled responses are very similar. From 5 to 8 s (50°C to 65°C), the response starts to reduce owing to the damping increment caused by viscoelastic effects. After 8 s, when the joint core material reaches the transition temperature, acceleration and displacement response become very similar to those obtained by applying a constant thermal load set to 65°C. Referring to Table 9, if the ground acceleration peaks before the joint core material reaches the transition temperature, such as the case under El Centro earthquake, control time delays have a significant effect on control performance. In this case, control performance is significantly lower than that obtained with the assumption of time-constant (instantaneous) thermal load. Otherwise, for example under Kobe and Chichi earthquakes, time delays have a much smaller effect on control performance, especially with regard to the normed control response. Note that a transition temperature of 65°C is specific to the type of SMP that is adopted in this study. However, existing SMP materials feature a transition temperature that varies from 10°C to 178°C.[38,39] Control time delay due to heating could be significantly reduced by choosing an SMP material with a lower transition temperature as well as a more efficient thermal actuation system.

6 | DISCUSSION

Time delays due to excitation detection and joint thermal actuation have been considered through simulation on the full-scale model. Generally, when considering time delay, vibration suppression becomes effective once the joint core material enters the viscoelastic region. However, control time delays significantly affect control performance if the ground acceleration peaks before the joint core material reaches the transition temperature. Control time delays due to joint

TABLE 9 Full-scale model: Control performance through adaptive structural joints considering time delay

Earthquake		El Centro Full-scale	El Centro Full-scale time delay	Kobe Full-scale	Kobe Full-scale time delay	Chichi Full-scale	Chichi Full-scale time delay	Kocaeli (60°C) Full-scale	Kocaeli (60°C) Full-scale time delay
J_1 (peak displacement)	1S	0.42	0.99	0.67	0.94	0.75	0.75	1.10	1.19
	2S	0.54	1.01	0.88	1.20	0.97	0.96	1.26	1.37
	3S	0.59	1.02	0.94	1.29	1.02	1.01	1.31	1.44
J_2 (peak drift ratio)	1S&2S	0.61	1.03	0.98	1.34	1.07	1.06	1.33	1.45
	2S&3S	0.66	1.05	1.28	1.49	1.21	1.20	1.34	1.42
J_3 (peak acceleration)	1S	0.81	0.98	0.88	0.78	0.81	0.80	0.89	0.99
	2S	0.51	0.97	0.83	0.89	0.78	0.79	0.84	0.84
	3S	0.44	1.04	0.81	0.83	0.79	0.80	0.78	0.87
J_4 (peak base shear)		0.31	0.95	0.55	0.77	0.73	0.74	0.89	0.99
J_5 (peak skin stress)		0.60	1.00	1.00	1.36	1.08	1.07	1.36	1.49
J_{1n} (normed displacement)	1S	0.57	0.88	0.59	0.66	0.97	0.93	1.15	1.20
	2S	0.71	0.94	0.72	0.79	1.21	1.15	1.31	1.35
	3S	0.76	0.96	0.77	0.83	1.29	1.23	1.36	1.40
J_{2n} (normed drift ratio)	1S&2S	0.79	0.97	0.80	0.86	1.34	1.28	1.40	1.44
	2S&3S	0.90	1.01	0.90	0.95	1.48	1.41	1.48	1.51
J_{3n} (normed acceleration)	1S	0.87	0.94	0.65	0.73	0.89	0.86	0.94	0.96
	2S	0.52	0.84	0.55	0.60	0.75	0.73	0.93	1.01
	3S	0.50	0.83	0.48	0.58	0.76	0.73	0.94	1.03
J_{4n} (normed base shear)		0.43	0.82	0.44	0.52	0.73	0.71	0.93	1.01
J_{5n} (normed skin stress)		1.05	1.12	1.03	1.03	1.87	1.69	1.46	1.46

thermal actuation can be drastically reduced by adopting an SMP material whose transition temperature is chosen to minimize control effort and energy requirements by limiting interference with field temperature and the effect of seasonal temperature variation.

Interference with field temperature may become of critical importance in the event of a fire. Note that the composite skin that reinforces the adaptive joints contains aramid (Kevlar) fabrics that are typically employed for fireproofing.[40] In addition, other thermal insulation solutions might be considered to satisfy fire safety criteria. For example, fire retardant coatings and cladding that are typically used for steel structures[41] could be applied to the adaptive joints considered in this work.

7 | CONCLUSIONS

This paper has presented numerical and experimental studies on a new semi-active response control strategy. A three-story frame equipped with 12 variable stiffness and damping joints has been taken under consideration. Joint thermal actuation causes a shift of the structure natural frequency and a parallel increase of damping, which has been effectively applied to mitigate the structure response under resonance and seismic excitations.

Simulations on a 1/10-scale three-story frame have shown that semi-active response control through variable stiffness and damping structural joints is effective to reduce acceleration and base shear under several seismic loadings. For the SMP material considered in this work, control performance is maximized when the joints are thermally actuated in the range 60°C–65°C. Peak acceleration and base shear are significantly reduced by up to 62% and 65%, respectively. Depending on the excitation characteristics, frequency shift might have a positive or negative effect on the structure dynamic response, which affects control performance. When the structure frequencies shift in a range in which the seismic loading has high

energy components, control performance might degrade, especially with regard to displacement and interstory drift due to the structure stiffness reduction. Nonetheless, because the effect of damping becomes dominant when the joints are thermally actuated to the transition region (above 50°C for the SMP employed in this work), acceleration and base shear response are reduced significantly in all cases. Experimental testing results are generally in good accordance with numerical predictions. Shake-table tests on a 1/10-scale prototype have confirmed that through thermal actuation of the joints, the structural damping ratio increases from 2.6% to 11.3% and the first modal frequency shifts by up to 37%. As the structure becomes more flexible, an increase of displacements and interstory drift might occur. However, depending on the seismic excitation, top-story acceleration and base shear are significantly reduced in the range 43%–50% and 35%–51%, respectively.

Future work could look into improving the adaptive joint thermal actuation system to reduce the time it takes to actuate the core to the transition temperature. For example, resistive heating efficiency could be improved by embedding carbon fibers/nanotubes, carbon black, or other conductive materials in either the reinforcement skin or the joint core matrix material. Inductive heating could also be tested by embedding magnetic particles such as Fe(III) oxide in the core matrix material. Better insulation solutions could also be implemented to minimize interference with field temperature, which will improve control efficiency and will enable satisfy fire safety criteria.

In order to generalize the conclusions reached in this paper, future work could also look into applying response control through variable stiffness and damping components to different structural configurations (e.g., plates, shells) as well as to frame structures with a more complex layout.

DATA AVAILABILITY STATEMENT
All data generated for this study are included in the article and supplementary material.

ORCID
Qinyu Wang https://orcid.org/0000-0002-0688-1887
Gennaro Senatore https://orcid.org/0000-0001-7418-9713

REFERENCES
1. Soong TT, Spencer BF. Active, semi-active and hybrid control of structures. *Bull N Z Soc Earthq Eng*. 2000;33(3):387-402.
2. Spencer BF Jr, Nagarajaiah S. State of the art of structural control. *J Struct Eng*. 2003;129(7):845-856.
3. Saaed TE, Nikolakopoulos G, Jnasson J-E, Hedlund H. A state-of-the-art review of structural control systems. *J Vib Control*. 2015;21(5):919-937.
4. Huang B, Zhang H, Wang H, Song G. Passive base isolation with superelastic nitinol SMA helical springs. *Smart Mater Struct*. 2014;23(6):065009.
5. Kasai K, Fu Y, Watanabe A. Passive control systems for seismic damage mitigation. *J Struct Eng*. 1998;124(5):501-512.
6. Ohtori Y, Christenson RE, Spencer BF Jr, Dyke SJ. Benchmark control problems for seismically excited nonlinear buildings. *J Eng Mech*. 2004;130(4):366-385.
7. Yang JN, Agrawal AK, Samali B, Wu JC. Benchmark problem for response control of wind-excited tall buildings. *J Eng Mech*. 2004;130(4):437-446.
8. Reinhorn AM, Soong TT, Riley MA, Lin RC, Aizawa S, Higashino M. Full-scale implementation of active control. II: Installation and performance. *J Struct Eng*. 1993;119(6):1935-1960.
9. Mirfakhraei SF, Andalib G, Chan R. Numerical investigation on toggled actuator forces in active vibration control system. *Adv Res Civ Eng*. 2019;1(2):16-35.
10. Wang L, Wang X, Li Y, Lin G, Qiu Z. Structural time-dependent reliability assessment of the vibration active control system with unknown-but-bounded uncertainties. *Struct Control Health Monit*. 2017;24(10):e1965.
11. Harvey PS Jr, Gavin HP, Scruggs JT, Rinker JM. Determining the physical limits on semi-active control performance: a tutorial. *Struct Control Health Monit*. 2014;21(5):803-816.
12. Symans MD, Constantinou MC. Semi-active control systems for seismic protection of structures: a state-of-the-art review. *Eng Struct*. 1999;21(6):469-487.
13. Arani AG, BabaAkbar-Zarei H, Jamali SA. Application of smart electro-rheological dampers in semi-active control of electro-rheological sandwich plates with nanocomposite facesheets rested on orthotropic visco-Pasternak foundation. *J Braz Soc Mech Sci Eng*. 2019;41(10):426.
14. Zhao YL, Xu ZD, Wang C. Wind vibration control of stay cables using magnetorheological dampers under optimal equivalent control algorithm. *J Sound Vib*. 2019;443:732-747.

15. Nagarajaiah S. Adaptive passive, semiactive, smart tuned mass dampers: identification and control using empirical mode decomposition, Hilbert transform, and short-term Fourier transform. *Struct Control Health Monit*. 2009;16(7-8):800-841.

16. Sun C, Nagarajaiah S. Study on semi-active tuned mass damper with variable damping and stiffness under seismic excitations. *Struct Control Health Monit*. 2014;21(6):890-906.

17. Gkatzogias KI, Kappos AJ. Semi-active control systems in bridge engineering: a review of the current state of practice. *Struct Eng Int*. 2016;26(4):290-300.

18. Teuffel P. *Entwerfen Adaptiver Strukturen* [Doctoral dissertation]. Struttgart: University of Stuttgart - ILEK; 2004.

19. Sobek W. Ultra-lightweight construction. *Int J Space Struct*. 2016;31(1):74-80.

20. Böhm M, Wagner J, Steffen S, Sobek W, Sawodny O. Homogenizability of element utilization in adaptive structures. In: 2019 IEEE 15th International Conference on Automation Science and Engineering (CASE); Vancouver: 2019:1263-1268.

21. Senatore G, Duffour P, Winslow P. Synthesis of minimum energy adaptive structures. *Structural and Multidisciplinary Optimization*. 2019;60(3):849–877. https://doi.org/10.1007/s00158-019-02224-8

22. Wang Y, Senatore G. Minimum energy adaptive structures - all-in-one problem formulation. *Comput Struct*. 2020;236:106266. https://doi.org/10.1016/j.compstruc.2020.106266

23. Senatore G, Duffour P, Winslow P, Wise C. Shape control and whole-life energy assessment of an "infinitely stiff" prototype adaptive structure. *Smart Mater Struct*. 2018;27(1):015022. https://doi.org/10.1088/1361-665X/aa8cb8

24. Reksowardojo AP, Senatore G, Smith IFC. Experimental testing of a small-scale truss beam that adapts to loads through large shape changes. *Front Built Environ*. 2019;5(93). http://doi.org/10.3389/fbuil.2019.00093

25. Senatore G, Reksowardojo AP. Force and shape control strategies for minimum energy adaptive structures. *Front Built Environ*. 2020;6(105). https://doi.org/10.3389/fbuil.2020.00105

26. Reksowardojo AP, Senatore G, Smith IFC. Design of structures that adapt to loads through large shape changes. *J Struct Eng*. 2020;146(5):04020068. https://doi.org/10.1061/(ASCE)ST.1943-541X.0002604

27. Senatore G, Wang Q, Bier H, Teuffel P. *The Use of Variable Stiffness Joints in Adaptive Structures*. Hamburg: International Association for Shells and Spatial Structures (IASS); 2017.

28. Wang Q, Senatore G, Jansen K, Habraken A, Teuffel P. Design and characterization of variable stiffness structural joints. *Mater Des*. 2020a;187:108353. https://doi.org/10.1016/j.matdes.2019.108353

29. Wang Q, Senatore G, Jansen K, Habraken A, Teuffel P. Vibration suppression through variable stiffness and damping structural joints. *Front Built Environ*. 2020b;6:550864. https://doi.org/10.3389/fbuil.2020.550864

30. Kobori T, Takahashi M, Nasu T, Niwa N, Ogasawara K. Seismic response controlled structure with active variable stiffness system. *Earthq Eng Struct Dyn*. 1993;22(1):925-941.

31. Pasala DTR, Sarlis AA, Nagarajaiah S, Reinhorn AM, Constantinou MC, Taylor D. Adaptive negative stiffness: new structural modification approach for seismic protection. *J Struct Eng*. 2013;139(7):1112-1123.

32. Shu Z, Zhang J, Nagarajaiah S. Dimensional analysis of inelastic structures with negative stiffness and supplemental damping devices. *J Struct Eng*. 2017;143(3):04016184.

33. Hu J, Chen W, Fan P, et al. Epoxy shape memory polymer (SMP): material preparation, uniaxial tensile tests and dynamic mechanical analysis. *Polym Test*. 2017;62:335-341.

34. Menard KP. *Dynamic Mechanical Analysis: a Practical Introduction*. Boca Raton: CRC Press; 2008.

35. ISO-6721-1. *Plastics Determination of Dynamic Mechanical Properties - ISO 6721-1*, Geneva: ISO; 2011.

36. Nakamura N. Extended Rayleigh damping model. *Front Built Environ*. 2016;2(14). https://doi.org/10.3389/fbuil.2016.00014

37. Carvalho E. Seismic testing of structures. In: *Earthquake Engineering-Invited Papers: Proceedings of the Eleventh European Conference*. Vol 2. 1999:53.

38. Takahashi T, Hayashi N, Hayashi S. Structure and properties of shape-memory polyurethane block copolymers. *J Appl Polym Sci*. 1996;60(7):1061-1069.

39. Kumar KS, Khatwa AK, Nair CR. High transition temperature shape memory polymers (SMPs) by telechelic oligomer approach. *React Funct Polym*. 2014;78:7-13.

40. Brown JR, Ennis BC. Thermal analysis of Nomex and Kevlar fibers. *Text Res J*. 1977;47(1):62-66.

41. CEN. *Eurocode 3 Design of Steel Structures - Part 1–2: General Rules - Structural Fire Design*. 2009.

SUPPORTING INFORMATION

Additional supporting information may be found online in the Supporting Information section at the end of the article.